PHYSICAL REVIEW APPLIED **17,** 064065 (2022)

Measuring the Gradient of Sound Pressure Directly Via Flexoelectricity

Zhaoqi Li,[1] Qian Deng,[2,*] and Shengping Shen[1,†]

[1] *State Key Laboratory for Strength and Vibration of Mechanical Structures, School of Aerospace, Xi'an Jiaotong University, Xi'an, Shaanxi 710049, China*

[2] *School of Aerospace Engineering, Huazhong University of Science and Technology, Wuhan 430074, China*

(Received 5 November 2021; revised 3 March 2022; accepted 13 June 2022; published 30 June 2022)

In this work, we propose the design of a flexoelectric sensor, which can measure sound-pressure gradient directly. It is found that the sensitivity of sound-pressure gradient of the flexoelectric sensor has a wide band for low working frequencies. Our theoretical and experimental results indicate that the position of sound sources can be predicted based on the measured sound-pressure gradients of three flexoelectric sensors, which are perpendicular to each other. Moreover, different from the previous design for a piezoelectric sensor array, only three flexoelectric sensors are needed to determine the orientation of sound sources. The flexoelectric sensor proposed here may provide an alternative way for the pressure-gradient measurement.

DOI: 10.1103/PhysRevApplied.17.064065

I. INTRODUCTION

In the deep ocean, due to physical constrictions to waves' propagation (large dissipation for high-frequency waves), optical, electric, and magnetic systems are only utilized for short-distance (< 100 m) communication [1,2]. Therefore, low-frequency sound waves are thought to be the only reliable long-distance signal carriers, which can propagate over thousands of kilometers in the deep sound channel [3]. However, the acoustic characters for various underwater targets are complex [4,5]. To accurately detect the targets, it is necessary to fully understand the feature of sound waves at the measuring point. Thus, not only the amplitude, but also the propagation direction of sound waves need to be measured [6–8]. Actually, how to accurately detect sound waves' propagation direction and design sensors with high quality are two of the most urgent tasks for underwater detection.

In the underwater environment, acoustic signals generated by targets can be simplified as plane waves propagating from far field. Assuming that the propagation of these plane waves is continuous, then the corresponding sound pressure p can be treated as a continuous function of space (x_1, x_2, x_3) and time t, i.e., $p(x_1, x_2, x_3, t)$. In practice, we always want to accurately measure the pressure field using measuring points as small as possible. If we only have one measuring point N_0 whose position is (X_0, Y_0, Z_0), by Taylor-series expansion, $p(x_1, x_2, x_3, t)$ can be expressed by the sound pressure and sound-pressure gradient measured at the point N_0 [9] as

$$\begin{aligned} p(x_1, x_2, x_3, t) &= p(N_0) + (x_1 - X_0)\frac{\partial p(N_0)}{\partial x_1} + (x_2 - Y_0)\frac{\partial p(N_0)}{\partial x_2} \\ &+ (x_3 - Z_0)\frac{\partial p(N_0)}{\partial x_3} \\ &+ o\left(\sqrt{\left(\frac{\partial p(N_0)}{\partial x_1}\right)^2 + \left(\frac{\partial p(N_0)}{\partial x_2}\right)^2 + \left(\frac{\partial p(N_0)}{\partial x_3}\right)^2}\right). \end{aligned} \quad (1)$$

In the close vicinity of N_0, higher-order gradients of the sound pressure is very small and can be simply ignored. Thus, the completed sound-field information at N_0 contains the sound pressure $p(N_0)$ and three linear independent sound-pressure gradients $\partial p(N_0)/\partial x_1$, $\partial p(N_0)/\partial x_2$, $\partial p(N_0)/\partial x_3$. With these measurements, the propagation direction and distance can be directly estimated.

Although the theoretical mechanism for sound-field estimation is straightforward, in practice, measuring pressure gradients is not trivial. In previous studies [10], sound-pressure gradients are calculated indirectly from the sound pressure measured at different points. For instance, with the sound pressure $p(N_1)$, $p(N_2)$ measured at points N_1 and N_2, the sound-pressure gradient along N_1N_2 direction may be estimated by the equation $p(N_2) - p(N_1)/|N_2N_1|$, where $|N_2N_1|$ is the distance between points N_2 and N_1. To obtain more accurate measurement for sound-pressure gradient, sensors need to be arranged in arrays as shown in Fig. 1. In pace with the increase of the number of sensors,

---

[*] tonydqian@hust.edu.cn

[†] sshen@mail.xjtu.edu.cn

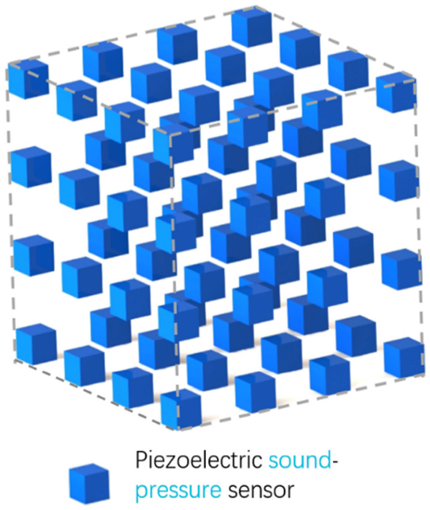

FIG. 1. The sound pressure sensor arrange multiple piezoelectric sensor together. Through measurements of those sound pressures, sound pressure gradients can be calculated.

the accuracy increases, while the size of array is inevitably enlarged. So that it is necessary to find out alternative kinds of sensors, which can measure the sound-pressure gradients directly.

In this paper, we propose a sound-pressure gradient sensor based on the flexoelectric effect. The governing equations of piezoelectric and flexoelectric sensors are solved, and the advantages of a flexoelectric sensor in directly measuring sound-pressure gradient are shown, both theoretically and experimentally. This paper is organized as follows: in Sec. II, we theoretically analyze the piezoelectric and flexoelectric sensors, and compare their performance in measuring sound-pressure gradients. In Sec. III, through simulations and experiments, we verify the performance of both a single flexoelectric sensor and a system of three flexoelectric sensors. Conclusions are drawn in Sec. IV.

II. MATHEMATICAL FORMULATION OF THE PIEZOELECTRIC SENSOR AND THE FLEXOELECTRIC SENSOR

A. The piezoelectric sensor

Piezoelectric materials have been widely used to measure the sound pressure due to their ability of generating electrical polarization in response to a uniform strain [11–14]. The piezoelectric effect can be expressed as

$$P_i = e_{ijk} S_{jk}, \tag{2}$$

where P_i, e_{ijk}, S_{jk} are the electric polarization, piezoelectric stress coefficient, and strain, respectively.

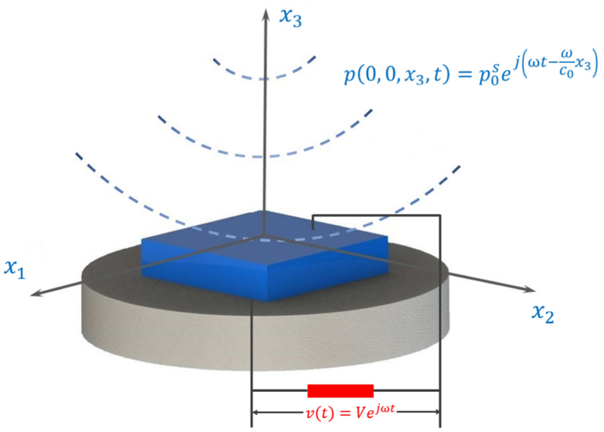

FIG. 2. This is a traditional piezoelectric sound-pressure sensor. The upper and lower surfaces of the model are coated with electrodes and connected in series with a resistor. When the excitation sound wave $p(0,0,x_3,t)$ propagates to the sensor, the voltage $v(t)$ is output across the external resistor R.

To illustrate the working mechanism of piezoelectric sensors, a traditional sound-pressure sensor model is schematically drawn in Fig. 2. As shown in the figure, the sensor contains a piezoelectric block fixed on a substrate. Both upper and lower surfaces of the piezoelectric block are coated by electrodes and connected with a resistor R. For simplicity, in the following analysis, only the deformation and polarization along x_3 direction are considered. Sound waves are supposed to be plane waves propagating along x_3 direction to the sensor. The sound pressure $p(x_1,x_2,x_3,t)$ can be expressed as follows [15–17]:

$$p(0,0,x_3,t) = P_0^S e^{j(\omega t-(\omega/c_0)x_3)}, \tag{3}$$

where P_0^S is the amplitude of $p(0,0,x_3,t)$, ω is the angular frequency, c_0 is the wave velocity in the medium, j is an imaginary unit. The response of the piezoelectric sensor can be measured as voltages $v(t)$ whose amplitude V is proportional to the amplitudes of the sound wave according to the following expressions (detailed calculations are given in appendix A):

$$\begin{aligned} B &= \left[\left(-\omega^2 M^p + K^p\right)\left(j\omega C_f^p + \frac{1}{R}\right) + j\omega(\Theta^p)^2\right]^{-1} \\ &\quad \times \left(j\omega C_f^p + \frac{1}{R}\right) P_0^S l^2 \\ V &= j\omega\left(j\omega C_f^p + \frac{1}{R}\right)^{-1} \Theta^p B, \end{aligned} \tag{4}$$

where V, B are amplitudes of output voltage and deflection of the block, R and l are the resistance and the length of the block, M^p, K^p, Θ^p, and C_f^p are parameters, which are also obtained in Eq. (A19).

Sound-pressure sensitivity level M_{fl} is usually used to evaluate the performance of a piezoelectric sensor [18].

The definition of M_{fl} is

$$M_{fl} = 20\log_{10}\frac{M_f}{M_r} = 20\log_{10}\frac{|V/P_0^S|}{M_r}, \qquad (5)$$

where $M_f = |V/P_0^S|$ is the sound-pressure sensitivity, M_r is a predefined reference level for M_f. $M_r = 1\ \mathrm{V}/\mu\mathrm{Pa}$ means 1 μPa sound pressure applied to the reference sensor can result in an output voltage of 1 V.

A pressure sensor with high quality needs a broad working band with frequency independent, which means that M_{fl} should be a constant value in the working frequency range. By substituting V obtained from Eq. (4) into Eq. (5), one may obtain the sound-pressure sensitivity level M_{fl}. In most cases, the reference level M_r is much larger than M_f. Thus, M_{fl} is usually negative; higher M_{fl} means a better performance of the sensor.

Now we theoretically calculate M_{fl} for piezoelectric sensors with different sizes and shapes. The sizes of the three sensors are $50 \times 100 \times 100\ \mathrm{mm}^3$, $500 \times 4000 \times 5000\ \mu\mathrm{m}^3$ and $1 \times 80 \times 100\ \mu\mathrm{m}^3$. Polyvinylidene tetrafluoroethylene (PVDF) is selected for the piezoelectric block. Material parameters for PVDF are given in Table I [19–21]. The sound-pressure sensitivity levels M_{fl} for the three models are plotted in Fig. 3. All three curves in Fig. 3 show that there are flat regions, representing frequency-independent domains, before the first-order resonant frequency. In practice, the sensor should work in the frequency-independent domain so that the measured sound pressure is reliable. Because of the flat regions, piezoelectric sensors are suitable for measuring sound pressure with the different geometries.

To explain why piezoelectric sensors are not suitable for measuring sound-pressure gradient, we propose an alternative parameter, sound-pressure gradient sensitivity level G_{fl}, to examine their performance on this aspect. Similar to the definition of M_{fl} in Eq. (5), G_{fl} may be written as

$$G_{fl} = 20\log_{10}\frac{G_f}{G_r} = 20\log_{10}\frac{|V/(-j\omega P_0^S/c_0)|}{G_r} \qquad (6)$$

where G_r is the reference level, $G_f = V/(-j\omega P_0^S/c_0)$ represents the sound-pressure gradient sensitivity along x_3 direction, which is defined based on Eq. (3).

TABLE I. PVDF parameters [19–21].

Symbols	Values	Symbols	Values
E (GPa)	3.70	g (N)	5×10^{-7}
ρ (kg/m^3)	1.78×10^3	a (Nm^2/C^2)	1.38×10^{10}
d_{33} (N/C)	1.02×10^9	f (Nm/C)	-179
P_0^S (N/m^2)	$0.0001/A$[a]	R $(M\Omega)$	20

[a] A is the area of the upper surface.

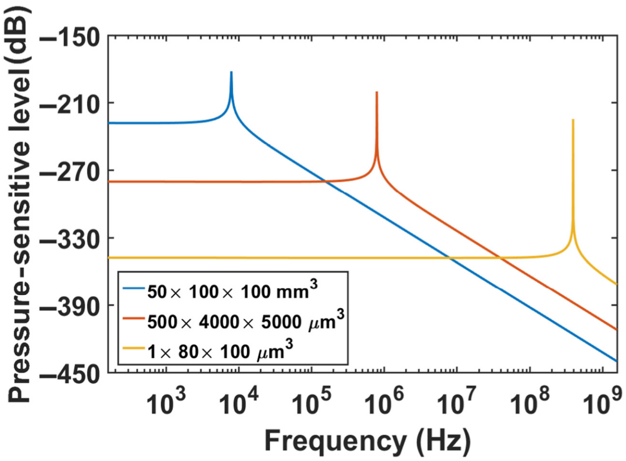

FIG. 3. Three M_{fl} curves of traditional sound-pressure sensor with the different ratios for thickness and length, and huge variations of geometries. Three curves all have a flat part before first-order resonant frequency, which means that piezoelectric sensors with different geometries are suitable for measuring the sound pressure.

By substituting Eqs. (3) and (4) into Eq. (6) and setting $G_r = 1\ \mathrm{Vm}/\mu\mathrm{Pa}$, we obtain the following equation, which is as same as Eq. (A42),

$$G_{fl} = 20\log_{10}\left\{|c_0\left(j\omega C_f^p + \frac{1}{R}\right)^{-1}\Theta^p \times \left[(-\omega^2 M^p + K^p)\left(j\omega C_f^p + \frac{1}{R}\right) + j\omega(\Theta^p)^2\right]^{-1} \times \left(j\omega C_f^p + \frac{1}{R}\right) l^2 |G_r^{-1}\right\}. \qquad (7)$$

The meaning of all parameters is given in Appendix A. G_{fl} curves for the three models described above are plotted in Fig. 4. In this figure, the sound-pressure gradient G_{fl} varies with the frequency without any flat region. The reason for this frequency dependency of G_{fl} can be found in Eq. (2). For the piezoelectric effect, the polarization $\mathbf{P}$ is related to the strain $\mathbf{S}$ linearly by the piezoelectric stress coefficient, so V is also related to the amplitude of external sound-pressure excitation P_0^S linearly. Thus, the quantity V/P_0^S in Eq. (5) is a constant before the resonant point. While for G_{fl}, as shown by Eq. (6), the relation between V and $\partial p/\partial x_3 = -j\omega P_0^S/c_0$ is not linear. Thus, using piezoelectric effect to measure sound-pressure gradients directly is not appropriate.

B. The flexoelectric sensor

Finding out a substitute for the piezoelectric sensor remains a challenging task. Fortunately, there is an alternative path for directly measuring sound-pressure gradients:

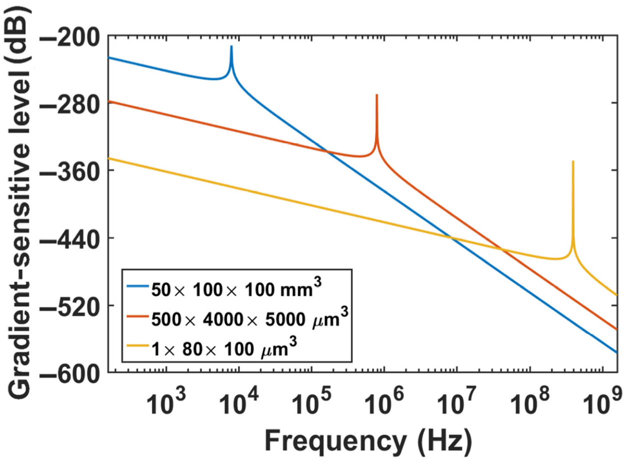

FIG. 4. Three G_{fl} curves of traditional sound pressure sensor, three sizes have the different ratios for thickness and length, and huge variations of geometries. All curves do not have flat part, which means that this kind of sensors are not suitable for measuring the sound pressure gradient.

the flexoelectric effect [22–24]. This is an electromechanical coupling between the polarization and strain gradient in all dielectric materials. Recent studies proposed several applications based on the flexoelectric effect [25–34]. The electric polarization, **P**, induced by the flexoelectric effect can be described as

$$P_i = \mu_{ijkl} \frac{\partial S_{jk}}{\partial x_l}, \tag{8}$$

where μ_{ijkl}, $\partial S_{jk}/\partial x_l$ are the flexoelectric coefficient, strain gradient. The strain gradient $\partial S_{jk}/\partial x_l$ of the sample changes as the external excitation sound-pressure gradient changes. Through the flexoelectric effect, we build a bridge between the pressure gradient and the polarization.

Motivated by the design for flexoelectric energy harvesting [27,29,35,36], we propose a flexoelectric beam-vector sensor shown by Fig. 5. Electrodes are coated on the upper and lower surfaces of the dielectric cantilever beam. This sensor would output a voltage $v(t)$ when there is a plane sound wave propagating perpendicular to the upper surface of the sensor. The vector sensor is fixed to receive the sound-pressure gradient along x_3 direction. The corresponding amplitude V of $v(t)$ in Eq. (A39) is shown as follows:

$$V = j\omega \left(j\omega C_f^f + \frac{1}{R} \right)^{-1} (-\Theta^f)$$
$$\times \left[-\omega^2 M^f + j\omega(\mu M^f + \gamma K^f) + K^f \right.$$
$$\left. + j\omega \left(j\omega C_f^f + \frac{1}{R} \right)^{-1} (\Theta^f)^2 \right]^{-1} P_0^S l^2$$

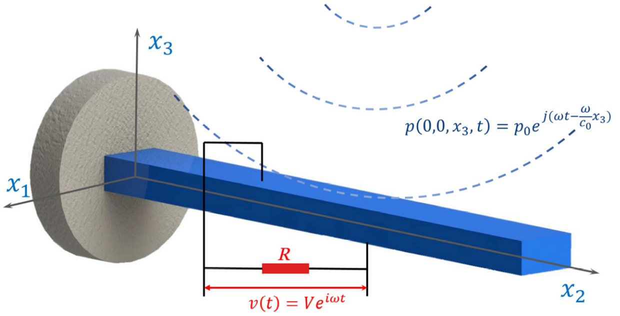

FIG. 5. Vector sensor model: the upper and lower surfaces of the model are coated with electrodes and connected in series with a resistor R. The output $v(t)$ is related to the sound-pressure gradient along x_3 direction.

$$B = \left[-\omega^2 M^f + j\omega(\mu M^f + \gamma K^f) + K^f \right]^{-1}$$
$$\times (P_0^S l^2 + \Theta^f V), \tag{9}$$

where V is the amplitude of output voltage, B is the generalized deflection amplitude of the beam, l is the length of the beam, M^f, K^f, Θ^f, and C_f^f are parameters obtained by the calculation in Eq. (A34), μ and γ are parameters related to resonant frequencies of the sensor in Eq. (A36).

Then, by substituting Eqs. (9) and (3) into Eq. (6), one may obtain the sound-pressure gradient sensitivity level G_{fl}, which is calculated in Eq. (A43)

$$G_{fl} = 20 \log_{10} \left\{ |c_0 \left(j\omega C_f^f + \frac{1}{R} \right)^{-1} (-\Theta^f) \right.$$
$$\times \left[-\omega^2 M^f + j\omega(\mu M^f + \gamma K^f) + K^f \right.$$
$$\left. \left. + j\omega \left(j\omega C_f^f + \frac{1}{R} \right)^{-1} (\Theta^f)^2 \right]^{-1} l^2 |G_r^{-1} \right\}. \tag{10}$$

As for the flexoelectric sensors, after obtaining G_{fl} in Eq. (10), we choose three models with different dimensions to plot both G_{fl} and M_{fl} curves. The sizes of the three sensors are 50 × 100 × 100 mm^3, 500 × 4000 × 5000 μm^3, and 1 × 80 × 100 μm^3, which are the same as the piezoelectric models. Material parameters for PVDF are the same as the piezoelectric models in Table I.

G_{fl} curves for the three models are plotted in Fig. 6(a). All curves in the figure show flat regions before the first-order resonant frequency, which means that the flexoelectric vector sensor proposed by Fig. 5 is suitable for measuring sound-pressure gradient. Three curves of the sound-pressure sensitivity level M_{fl} for models with different sizes are plotted in Fig. 6(b). All three curves in Fig. 6(a) change with the frequency. The M_{fl} values are not

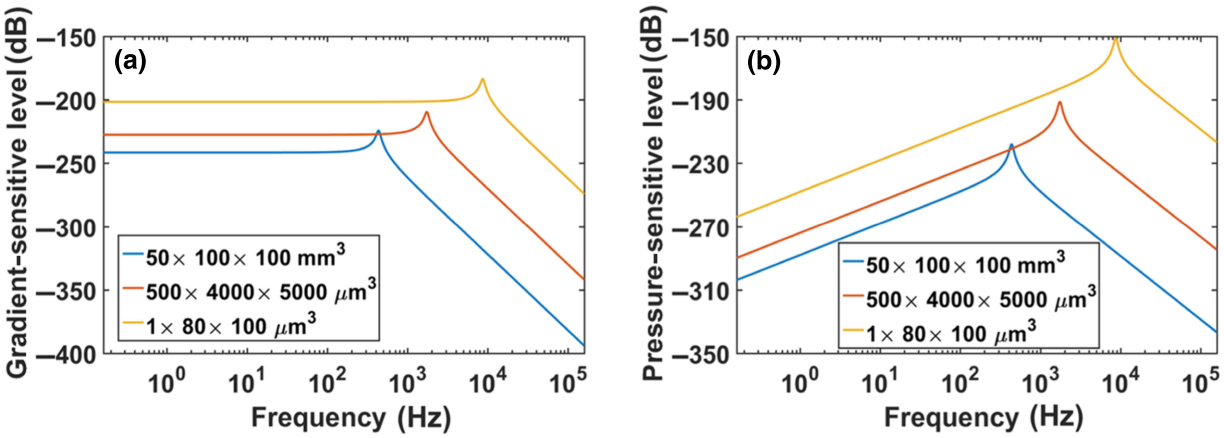

FIG. 6. (a) Three G_{fl} curves of vector sensors. (b) Three M_{fl} curves of vector sensors. Compared with the piezoelectric sensor, the vector sensor is suitable for measuring the sound pressure gradient.

constants, the sound pressure and the output do not fit the linear relationship further. Thus, using flexoelectric effect to measure sound pressure is not appropriate.

III. EXPERIMENTS AND SIMULATIONS

The flexoelectric sensor shows the advantages of measuring sound-pressure gradients in the previous section, which can be confirmed by relevant experiments. We select BST ($Ba_{0.67}Sr_{0.33}TiO_3$, the well-known best flexoelectric material in ferroelectrics, corresponding flexoelectric coefficient reach to 100 μC/m under its Curie point 20 °C [37], which operates stably at average surface temperature 16.1 °C of the oceans [38]. And the BST sample we use is nonpolarized and not affected by Curie point) as the experimental material, and the thickness, width and length for the beam are 2.5, 6, and 15 mm, respectively. The experimental process and the inner structure of the sensor are shown in Fig. 7.

The experimental process is as follows. Firstly, the transmitting transducer is placed in water. Through the signal generator and power amplifier, sinusoidal signals are transmitted with specific frequencies by the transducer in water. Then, the assembled single flexoelectric sensor and the piezoelectric sensor (B&K 8104) are placed at the same 1-m distance from the transducer. The same distance could ensure that the two sensors receive the sound wave with equal intensity. Finally, the electrical outputs of the two sensors are obtained through the oscilloscope.

From 1 to 10 kHz, the frequency spacing as 500 Hz, we select 19 measuring points and the amplitude of sound pressure at each measuring point is set as 2180 Pa. The G_{fl} points of various frequencies of the two sensors are scattered in Fig. 8.

B&K 8104 is a traditional piezoelectric sensor, and the measuring points of B&K have the consistent variation trend with the curves in Fig. 4. The result shows the same conclusion as theory calculation that piezoelectricity is not suitable for measuring sound-pressure gradient.

For the flexoelectric sensor, the measuring points are close to the horizontal line $G_{fl} = -182$ dB, but there are some deviations of measuring points. The deviation is mainly derived from the environment (the electromagnetic interference, ambient noise) and the manufacturing (handmade sample, signal processing device unused) errors. And the deviations would not influence the trends of G_{fl}, with sophisticated manufacturing and signal processing can reduce these errors. On the whole, our flexoelectric vector sensor is actually still in prototype phase, and the trend of the G_{fl} curve is consistent with the theoretical

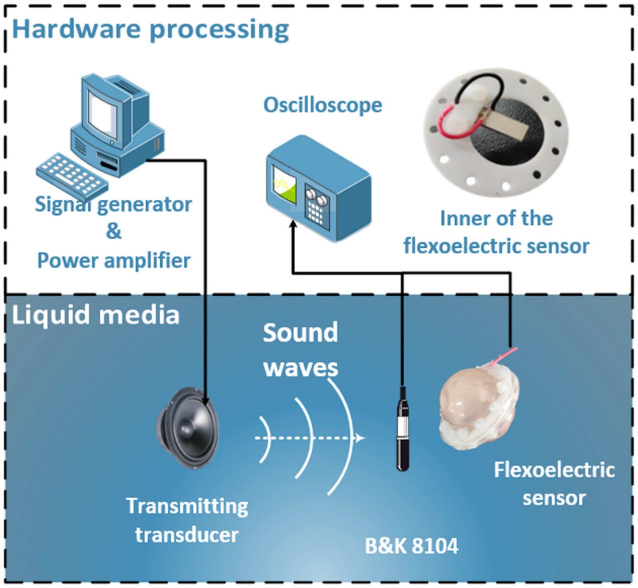

FIG. 7. Experiment for measuring the sound-pressure gradient sensitivity level G_{fl} of the flexoelectric sensor and the inner structure of the sensor.

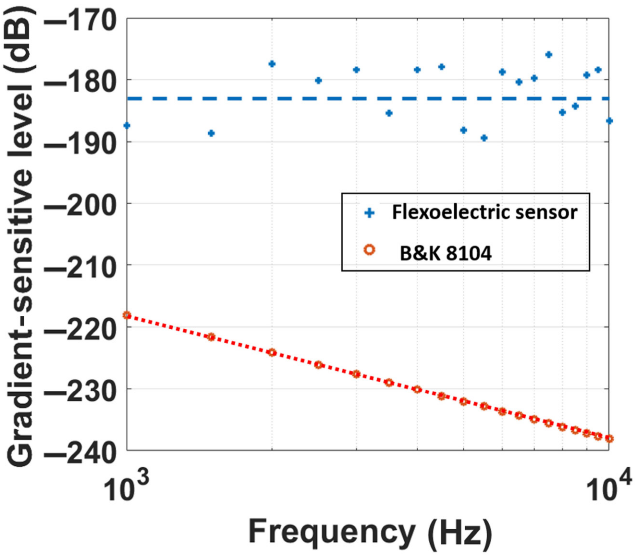

FIG. 8. Measuring G_{fl} points of the piezoelectric sensor and the flexoelectric sensor ($G_r = 1/2\pi$ Vm/μPa).

prediction. The advantages of measuring sound-pressure gradient with flexoelectricity are apparent with frequency independence.

In Fig. 8, we also find that in the measured frequency band, under the same excitation, the output voltage of the flexoelectric sensor is always much higher than that of the piezoelectric sensor. Such high output is all due to the larger deformation of the cantilever structure under the same excitation than that of the block structure. The experimental results prove that the flexoelectric sensor has a lower excitation threshold, that is, it can detect weaker sound waves.

To determine the direction of underwater objects, three-vector flexoelectric sensors are placed along three perpendicular directions as shown in Fig. 9. Using such a system, the propagation directions of specific waves can be determined. We use the following example to demonstrate this point. Assume there are five plane waves with different frequencies transmitting from different directions to the measuring point. Due to the difference in frequencies, there should be no interference between them. Their propagation directions are (1, 0, 0), (1, 1, 1), (1, 2, 1), (0, 1, 1), and (0, 0, 1). The total sound pressure can be expressed as follows:

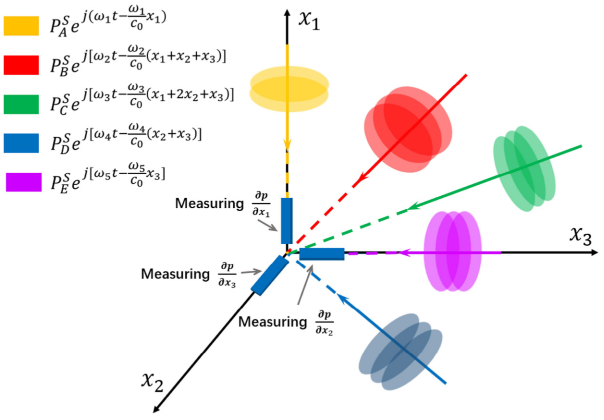

FIG. 9. Total sound pressure at the (0, 0, 0) point is superimposed by five plane waves shown by different colors. Three flexoelectric vector sensors are utilized to measure sound-pressure gradients $\partial p/\partial x_1$, $\partial p/\partial x_2$, $\partial p/\partial x_3$ from three directions.

$$p = P_A^S e^{j(\omega_1 t - (\omega_1/c_0)x_1)} + p_B^S e^{j(\omega_2 t - (\omega_2/c_0)(x_1+x_2+x_3))} + P_C^S e^{j(\omega_3 t - (\omega_3/c_0)(x_1+2x_2+x_3))} + P_D^S e^{j(\omega_4 t - (\omega_4/c_0)(x_2+x_3))} + P_E^S e^{j(\omega_5 t - (\omega_5/c_0)x_3)}, \quad (11)$$

where P_A^S, P_B^S, P_C^S, P_D^S, P_E^S are five sound-pressure amplitudes along five directions, $\omega_1 = 2\pi f_1 = 100$ rad/s, $\omega_2 = 2\pi f_2 = 200$ rad/s, $\omega_3 = 2\pi f_3 = 300$ rad/s, $\omega_4 = 2\pi f_4 = 400$ rad/s, $\omega_5 = 2\pi f_5 = 500$ rad/s are the corresponding angular frequencies. Assume that the relationship between five acoustic pressure amplitudes is $P_A^S = P_B^S = P_C^S = P_D^S = P_E^S = 2$ Pa. The total excitation is

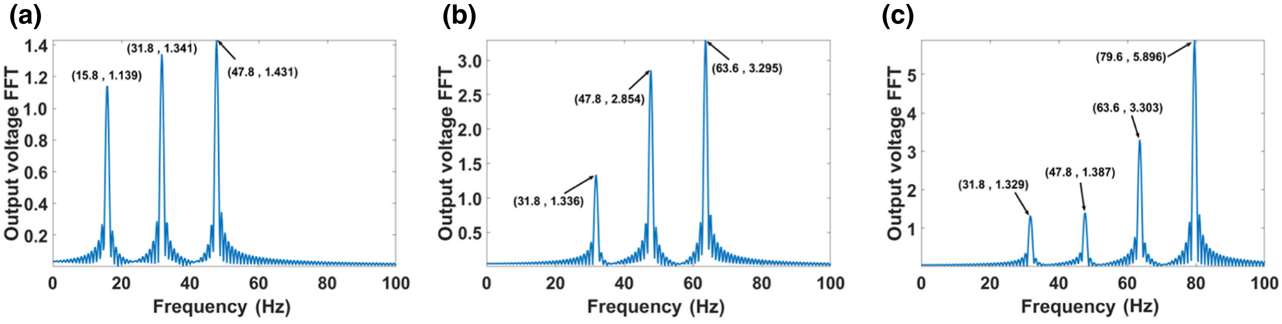

FIG. 10. Fast Fourier transform (FFT) for the three-sensor output voltage signals. (a) The FFT curve for measuring $\partial p/\partial x_1$, which contains three main peaks with different frequencies: 15.8, 31.8, 47.8 Hz. (b) The FFT curve for measuring $\partial p/\partial x_2$, which contains three main peaks with different frequencies: 31.8, 47.8, 63.6 Hz. (c) The FFT curve for measuring $\partial p/\partial x_3$, which contains four main peaks with different frequencies: 31.8, 47.8, 63.6, 79.6 Hz.

TABLE II. Main peaks of FFT curves and estimated propagation directions.

Items	f_1(15.8 Hz)	f_2(31.8 Hz)	f_3(47.8 Hz)	f_4(63.6 Hz)	f_5(79.6 Hz)
$\partial p/x_1$	1.139	1.341	1.431	/	/
$\partial p/x_2$	/	1.336	2.854	3.295	/
$\partial p/x_3$	/	1.329	1.387	3.303	5.896
Estimated direction	(1, 0, 0)	(1, 0.99, 0.99)	(1, 1.99, 0.97)	(0, 1, 1)	(0, 0, 1)
Actual direction	(1, 0, 0)	(1, 1, 1)	(1, 2, 1)	(0, 1, 1)	(0, 0, 1)

the superposition of these five plane waves, so that output signals also contain different frequencies of these waves. After taking the fast Fourier transform [39] (FFT), frequency domain signals on separate frequencies are shown in Fig. 10.

In Fig. 10(a), the FFT curve shows the amplitude spectrum of $\partial p/\partial x_1$ in frequency domain, and the curve has three main peaks, which correspond to the frequencies of f_1, f_2, and f_3. Since the sound-pressure gradient $\partial p/\partial x_1$ of f_4 and f_5 is zero, there are no peaks with these two frequencies in the curve. The FFT curve in Fig. 10(b) shows the amplitude spectrum of $\partial p/\partial x_2$ in frequency domain with no contribution of gradients values of f_1 and f_5, the curve also has three main peaks, which correspond to f_2, f_3, and f_4. Similarly, the FFT curve in Fig. 10(c) shows the amplitude spectrum of $\partial p/\partial x_3$, with no contribution of gradient values of f_1, the curve has four main peaks, which correspond to f_2, f_3, f_4, and f_5.

All amplitudes of the peaks in Fig. 10 are listed in Table II. As depicted in the third column of Table II, amplitudes are 1.341, 1.336, and 1.329, which correspond to the proportions of sound-pressure gradients of the plane wave with the frequency of f_2. Through normalizing the three values, the source direction of the wave with the frequency

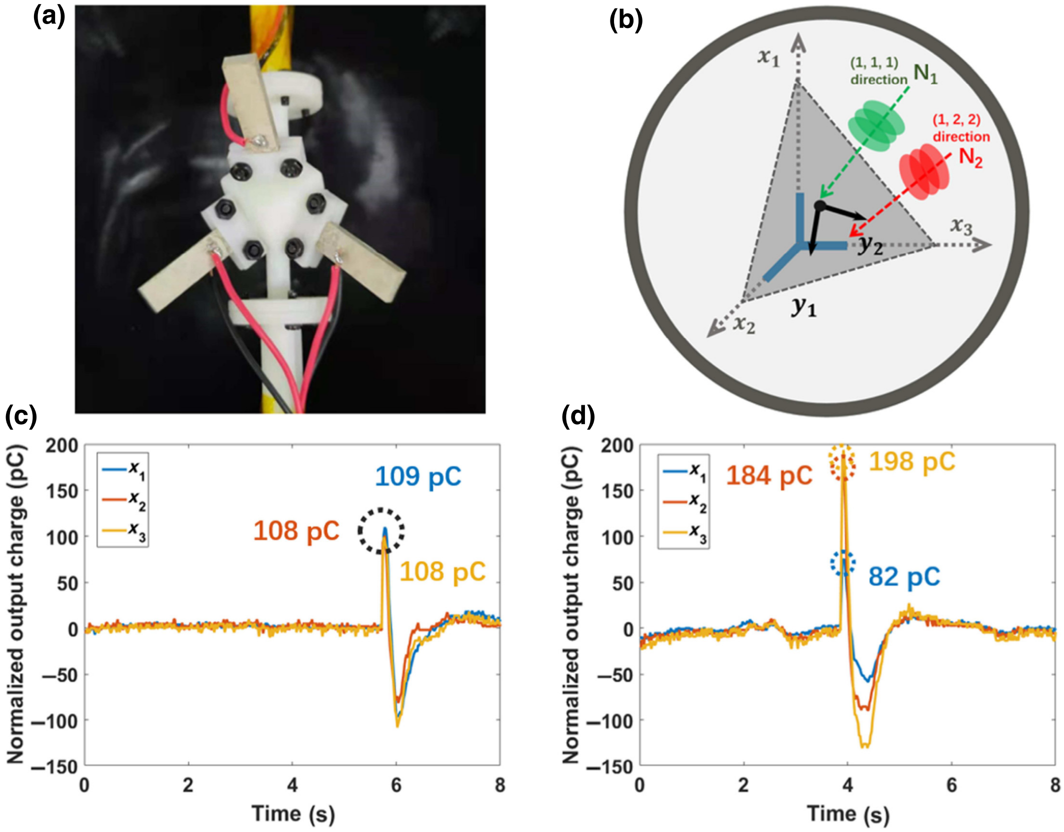

FIG. 11. (a) Three cantilever beams are assembled in a hollow rubber sphere which is full of castor oil and output the charge of upper and lower surfaces. (b) Two direction vectors $\mathbf{N_1}$ and $\mathbf{N_2}$ are marked in green and red, respectively. When knocking along $\mathbf{N_1}$ and $\mathbf{N_2}$ directions, the generated sound waves would transmit to the system. Plane-K $x_1 + x_2 + x_3 = 1$ mm is selected to display the results of estimated directions. (c) The normalized output associated with the knocking stimulation in $\mathbf{N_1}$ direction. (d) The normalized output associated with the knocking stimulation in $\mathbf{N_2}$ direction.

TABLE III. Output charge of the system and the intersections of plane K and the ratio of outputs.

	Output charge of the system			Intersections	
Unit	Q_1 (pC)	Q_2 (pC)	Q_3 (pC)	y_1 (mm)	y_2 (mm)
Knocking in (1,1,1) direction	109	108	108	0.0205	0.0141
	82	89	90	−0.0031	−0.0025
	91	78	72	−0.0386	−0.0400
	107	115	117	0.0176	0.0129
	110	108	112	−0.0031	0.0087
Knocking in (1,2,2) direction	82	184	198	0.1424	0.1589
	103	226	284	0.1563	0.1145
	96	203	207	0.1503	0.0929
	89	230	171	0.2038	0.0196
	72	188	202	0.1767	0.1275

of f_2 is estimated as $(1, 0.99, 0.99)$. The directions of other waves can also be estimated in the same way, the direction of the sound source estimated by the system are 15.8 Hz, $(1, 0, 0)$; 31.8 Hz, $(1, 0.99, 0.99)$; 47.8 Hz, $(1, 1.99, 0.97)$; 63.6 Hz, $(0, 1, 1)$; and 79.6 Hz, $(0, 0, 1)$. And the estimated directions are close to the assumption, which are 15.8 Hz, $(1, 0, 0)$; 31.8 Hz, $(1, 1, 1)$; 47.8 Hz, $(1, 2, 1)$; 63.6 Hz, $(1, 2, 1)$; and 79.6 Hz, $(0, 0, 1)$.

In principle, corresponding experiments would be more convincing to identify the sound source direction. Herein, three BST cantilever beams are assembled along three mutually perpendicular directions as the three-beam system shown in Fig. 11(a). The system is fixed inside a hollow rubber sphere filled with castor oil. The thickness, width, and length for each BST beam are 2.5, 6, and 15 mm, respectively. All three beams are calibrated, and the calibration process is described as below: we record the output of the three beams under 300 Hz 1000 Pa sinusoidal excitation, and normalize the amplitude of the output, that is, we ensure the output charges of the three beams are equal in the same conditions.

Next, as shown in Fig. 11(b), two directions $\mathbf{N_1}$ and $\mathbf{N_2}$ are marked in green and red. When we knock the spherical shell along green and red directions, the generated sound waves would be transmitted to the system along $\mathbf{N_1} : (x_1, x_2, x_3) = (1, 1, 1)$ and $\mathbf{N_2} : (x_1, x_2, x_3) = (1, 2, 2)$, respectively. A small steel hammer with weight 20 g is used in knocking. The distance between the knocking position and the three beams is 15 cm. The amplitude of background noise in experiment is 0.5 Pa, and the flexoelectric sensor is sensitive. As long as the excited sound-wave intensity is higher than the noise, the wave can be measured. Meanwhile, we select a plane $x_1 + x_2 + x_3 = 1$ mm [named as plane K, which is the triangular plane in Fig. 11(b)] and calculate the intersections of plane K and $\mathbf{N_1}$, $\mathbf{N_2}$ vectors. Through these intersections, each vector in the three-dimensional space can be converted into a point in the two-dimensional plane, which can be displayed distinctly. Furthermore, a coordination transformation

$$\begin{bmatrix} y_1 \\ y_2 \end{bmatrix} = \begin{bmatrix} -\frac{1}{\sqrt{2}} & \frac{1}{\sqrt{2}} & 0 \\ -\frac{1}{\sqrt{6}} & -\frac{1}{\sqrt{6}} & \frac{2}{\sqrt{6}} \end{bmatrix} \begin{bmatrix} x_1 \\ x_2 \\ x_3 \end{bmatrix}$$

of plane K is proposed. Through such transformation, the vectors $\mathbf{N_1}$ and $\mathbf{N_2}$ can be converted into points A_{N1} : (0 mm, 0 mm) and A_{N2} : (0.1414 mm, 0.0816 mm).

The curves in Figs. 11(c) and 11(d) represent the electrical outputs of knocking in $\mathbf{N_1}$ and $\mathbf{N_2}$ after calibration and the slight fluctuation of the curve is caused by noise. The main peaks of the curves reflect the knocked strength along three perpendicular directions. $Q_1 = 109$ pC, $Q_2 = 108$ pC, and $Q_3 = 108$ pC are the outputs of the system through knocking the shell in $\mathbf{N_1}$ direction, and the prediction $(x_1, x_2, x_3) = (1, 0.99, 0.99)$ is calculated from the ratio of Q_1, Q_2, and Q_3. Then, the position of the associated point in plane K is $(y_1, y_2) = (0.0205$ mm$, 0.0141$ mm$)$. Likewise, $Q_1 = 82$ pC, $Q_2 = 184$ pC and $Q_3 = 198$ pC are outputs of the system when knocking in $\mathbf{N_2}$ direction. The prediction is $(x_1, x_2, x_3) = (1, 2.24, 2.41)$, which is the

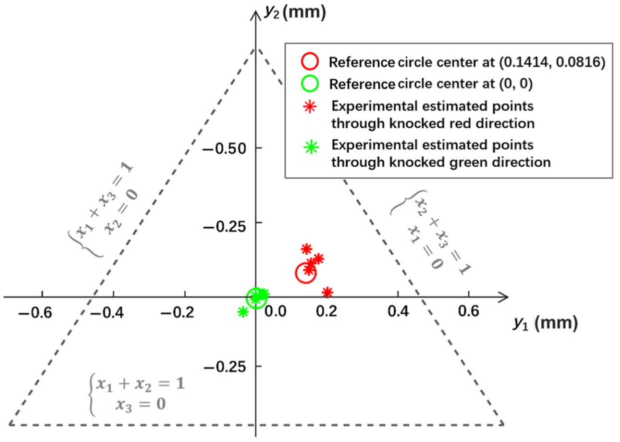

FIG. 12. Intersections and reference circles are plotted on plane $x_1 + x_2 + x_3 = 1$ mm.

ratio of Q_1, Q_2, and Q_3. The associated intersection points in plane K is $(y_1, y_2) = (0.1424\ \text{mm}, 0.1589\ \text{mm})$.

Further, we repeat the knocking of the spherical shell four more times along $\mathbf{N_1}$ and $\mathbf{N_2}$, respectively. All the outputs Q_1, Q_2, Q_3, and corresponding intersections are recorded in Table III. And the intersections are plotted in Fig. 12. Meanwhile, two circles, whose central coordinates are at A_{N1} and A_{N2}, are plotted as references in Fig. 12. In general, estimated intersections are close to the reference circles.

IV. CONCLUSION

In summary, based on the unique electromechanical coupling mode of the flexoelectric effect, we propose a flexoelectric sensor, which can measure sound-pressure gradient directly and show that its sound-pressure gradient sensitivity has a wide working frequency band. Moreover, based on the flexoelectric sound-pressure gradient sensor, we further propose a system to predict the position of sound sources based on the measured sound-pressure gradients. At last, the experiments are proposed to illustrate the concept of the flexoelectric sensor system. In general, our work provides an alternative perspective to underwater detection and design for flexoelectric vector sensor.

ACKNOWLEDGMENTS

We gratefully acknowledge the financial support from the National Key R&D Program of China (2017YFE0119800), the 111 Project of China (B18040).

APPENDIX: FORMULA DERIVATION FOR PIEZOELECTRIC AND FLEXOELECTRIC SENSORS

The total energy equation of the piezoelectric sensor or flexoelectric sensor can be derived from Hamilton's principle as

$$\delta \int_{t_1}^{t_2} L\, dt + \delta W = 0, \quad L = T - H, \tag{A1}$$

where T is the total kinematic energy, H is the total electric enthalpy, and W is the work done by the external forces.

The total kinematic energy T and the total electric enthalpy energy H can be expressed as

$$\begin{aligned} T &= \frac{1}{2}\int_V \rho \dot{u}_i \dot{u}_i\, dV, \\ H &= \int_V \left(U_b - \frac{1}{2}\epsilon_0 \phi_{,i}\phi_{,i} + \phi_{,i}P_i\right) dV, \end{aligned} \tag{A2}$$

where () and $(, i)$ represent partial derivative of time and partial derivative of coordinate i. V denotes the volume occupied by the model, ρ is the mass density of the solid. u_i and P_i are components of the displacement and polarization vectors. ϵ_0 is the permittivity of a vacuum and ϕ is a variation of potential due to the virtual work done by moving charges onto or out of the electrodes. U_b is the internal energy density.

The work done by the external forces can be expressed as

$$\delta W = \int_{t_1}^{t_2} \int_{\Omega^\pm} p\, \delta u_A\, dA\, dt, \tag{A3}$$

where $\Omega^\pm$ represent the upper and lower surface of the model. p is the external sound pressure. u_A is the generalized doing work distance of the sound pressure. A is the area of upper or lower surface of the sample.

The internal energy density is written as [27,35]

$$\begin{aligned} U_b = {} & \frac{1}{2}a_{kl}P_kP_l + \frac{1}{2}c_{ijkl}S_{ij}S_{kl} + d_{ijk}P_iS_{jk} + f_{ijkl}P_iS_{jk,l} \\ & + \frac{1}{2}g_{ijklmn}S_{ij,k}S_{lm,n}, \end{aligned} \tag{A4}$$

where $\mathbf{a}$, $\mathbf{c}$, $\mathbf{d}$, $\mathbf{f}$, and $\mathbf{g}$ are the material property tensors. In particular, $\mathbf{a}$ and $\mathbf{c}$ are the second-order reciprocal dielectric susceptibility and fourth-order elastic constant tensors, respectively. The tensor $\mathbf{g}$ represents the purely nonlocal elastic effects and relates to the strain gradient elastic theories. $\mathbf{d}$ and $\mathbf{f}$ are the piezoelectric strain coefficient and flexoelectric coefficient. $\mathbf{u}$ and $\mathbf{P}$ are the displacement and the polarization vectors, $\mathbf{S}$ is the strain tensor, which is defined as

$$S_{ij} = \frac{1}{2}(u_{i,j} + u_{j,i}). \tag{A5}$$

We assume the polarization P_3 is along the thickness direction, only P_3 is nonzero, which can be expressed as

$$P_3 = P(x_1, x_2, x_3, t). \tag{A6}$$

1. Piezoelectric bulk model

The lower surface with the electrode of the model is fixed, then assume that the external sound pressure p is a plane wave propagating along the normal vector direction $(0, 0, 1)$ of the upper surface. The displacement on the lower surface Ω^- is zero. The sound pressure transmitted to the upper surface Ω^+ can be expressed as

$$p(t) = P_0^S e^{j\omega t}. \tag{A7}$$

Since the sound pressure p is uniformly distributed on the upper surface of the model, we assume that the strain along

x_3 direction is also uniformly distributed. The displacement u_3 and S_{33} are shown as

$$u_3(x_3, t) = \frac{x_3}{h} b(t) \quad S_{33}(t) = \frac{\partial u_3}{\partial x_3} = \frac{1}{h} b(t), \tag{A8}$$

where $b(t)$ is the displacement of upper surface, h is the height of piezoelectric bulk. x_3 is the x_3-axis coordinates of any point inside the piezoelectric bulk. Since the deformation of the piezoelectric is uniform, all components of the strain gradient tensor $S_{ij,k}$ are zero, thus the last two terms in Eq. (A4) do not exist. For a piezoelectric bulk, substitute Eqs. (A6) and (A8) into Eq. (A4), the internal energy density is shown as

$$U_b = \frac{1}{2} a P_3^2 + \frac{1}{2} c_{33} S_{33}^2 - d_{33} P_3 S_{33}, \tag{A9}$$

where a is the reciprocal dielectric susceptibility in x_3 direction. $c_{33} = c_{3333}$, S_{33}, and $d_{33} = d_{333}$ are the elastic property, strain, and the piezoelectric constant in x_3 direction. With Eqs. (A2), (A3), (A7), and (A9), we can rewrite Eq. (A1) as

$$\begin{aligned} &\int_{t_1}^{t_2} dt \int_V \left\{ -\rho \ddot{u}_3 \delta u_3 - \left(a P_3 + d_{33} S_{33} + \frac{\partial \phi}{\partial x_3} \right) \delta P_3 \right. \\ &\quad \left. - (c_{33} S_{33} + d_{33} P_3) \delta S_{33} + \frac{\partial D_3}{\partial x_3} \delta \phi \right\} dV \\ &\quad + \int_{t_1}^{t_2} dt \int_{\Omega +} p \, \delta u_A \, dA = 0, \end{aligned} \tag{A10}$$

where $D_3 = -\epsilon_0(\partial \phi / \partial x_3) + P_3$ denotes the electric displacement in the bulk.

In Eq. (A10), δP is arbitrary, so we have

$$a P_3 - d_{33} S_{33} + \frac{\partial \phi}{\partial x_3} = 0 \tag{A11}$$

and Maxwell equation

$$\frac{\partial D_3}{\partial x_3} = 0. \tag{A12}$$

Substituting Eq. (A11) into Eq. (A12), we further have

$$\frac{\partial^2 \phi}{\partial x_3^2} = -\frac{\partial E_3}{\partial x_3} = 0, \tag{A13}$$

where E_3 is the component of electric field $\mathbf{E}$ in the x_3 direction. For the bulk coated with electrodes on the upper and lower surface of the sample. E_3 is the only nonzero component of $\mathbf{E}$. Equation (A13) indicates that the electric field is uniform across the thickness of the bulk, and it also means that assuming the displacement and strain like Eq. (A8) is reasonable. So the output voltage can simply be expressed as $E_3 = -v(t)/h$, where $v(t)$ is the voltage difference between upper and lower electrodes. Next, the term associated with δu_3 and δS_{33}, Eq. (A10) is rewritten as

$$\begin{aligned} &\int_{t_1}^{t_2} dt \int_V \left\{ -\rho \ddot{u}_3 \delta u_3 \right. \\ &\quad \left. - \left[c_{33} S_{33} - d_{33} \left(-\frac{1}{a} \frac{V(t)}{h} + \frac{d_{33} S_{33}}{a} \right) \right] \delta S_{33} \right\} dV \\ &\quad + \int_{t_1}^{t_2} dt \int_{\Omega +} p \, \delta u_A \, dA = 0. \end{aligned} \tag{A14}$$

The volume integral $\int_V (*) \, dV$ of the piezoelectric bulk can convert into the triple integral $\int_0^h \int_0^l \int_0^l (*) \, dx_2 \, dx_1 \, dx_3$, where l is the length and width of the piezoelectric bulk. The surface integral $\int_{\Omega +} (*) \, dA$ can convert into the double integral $\int_0^l \int_0^l (*) \, dx_2 \, dx_1$. Because p is applied to the upper surface of the model, the generalized doing work distance is shown as

$$u_A(t) = u_3(x_3, t)|_{x_3 = h} = b(t). \tag{A15}$$

We substitute Eqs. (A8), (A15) into Eq. (A14) and convert the volume and surface integrals to the triple and double integrals

$$\begin{aligned} &\int_{t_1}^{t_2} dt \int_0^h \int_0^l \int_0^l -\frac{\rho x_3^2}{h^2} \ddot{b} \delta b - \left(\frac{c_{33}}{h^2} + \frac{d_{33}^2}{a h^2} \right) b \delta b \\ &\quad + \frac{d_{33}}{a h^2} V \delta b \, dx_2 \, dx_1 \, dx_3 = -\int_{t_1}^{t_2} p l^2 \delta b \, dt. \end{aligned} \tag{A16}$$

The closed circuit indicates that the charge density moving between the two electrodes is equal to the electric displacement at the surface where the electrode attached to. That means, the current $i(t)$ flowing through the resistor R equals the rate of the average electric displacement D_3, the electrical governing equation is shown as

$$\begin{aligned} i(t) &= \frac{v(t)}{R} = \frac{1}{h} \frac{d}{dt} \int_V \left(-\epsilon_0 \frac{v(t)}{h} + P \right) dV \\ &= -\frac{l^2}{h} \left(\epsilon_0 + \frac{1}{a} \right) \dot{v}(t) + \frac{l^2 d_{33} S_{33}}{a}. \end{aligned} \tag{A17}$$

Equations (A14) and (A17) are the governing equations of the bulk, then substitute Eq. (A8) into these two equations to get ordinary differential equations:

$$\begin{aligned} &M^p \ddot{b}(t) + K^p b(t) + \Theta^p v(t) = -p(t) l^2, \\ &C_f^p \dot{v}(t) + \frac{v(t)}{R} - \Theta^p \dot{b}(t) = 0. \end{aligned} \tag{A18}$$

M^p, K^p, Θ^p, C_f^p are an equivalent mass parameter, stiffness parameter, piezoelectric coupling coefficients, and velocity coupling parameter, which are shown as

$$\begin{aligned}
M^p &= \int_0^h \rho l^2 \left(\frac{x_3}{h}\right)^2 dx_3 = \frac{\rho l^2 h}{3},\\
K^p &= \int_0^h l^2 \left(\frac{c}{h^2} - \frac{d_{33}^2}{ah^2}\right) dx_3 = \frac{l^2}{h}\left(c - \frac{d_{33}^2}{a}\right),\\
\Theta^p &= \int_0^h l^2 \frac{d_{33}}{ah^2} dx_3 = \frac{d_{33} l^2}{ah},\\
C_f^p &= \frac{l^2}{h}\left(\epsilon_0 + \frac{1}{a}\right).
\end{aligned} \tag{A19}$$

Since the sound-wave pressure $p(t) = P_0^S e^{j\omega t}$ is reasonable to assume as harmonic excitation with frequency ω. Thus, $b(t)$ and $v(t)$ under steady state can also be expressed as the harmonic response with frequency ω as follows:

$$b(t) = Be^{j\omega t}, \quad v(t) = Ve^{j\omega t}. \tag{A20}$$

Substituting Eqs. (A7) and (A20) into Eq. (A18), the unknowns amplitude B and V are obtained

$$\begin{aligned}
B &= \left[(-\omega^2 M^p + K^p)\left(j\omega C_f^p + \frac{1}{R}\right) + j\omega(\Theta^p)^2\right]^{-1}\\
&\quad \times \left(j\omega C_f^p + \frac{1}{R}\right) P_0^S l^2,\\
V &= j\omega\left(j\omega C_f^p + \frac{1}{R}\right)^{-1} \Theta^p B.
\end{aligned} \tag{A21}$$

To obtain the output V, the necessary parameters are: bulk density ρ, x_3 direction piezoelectric parameter d_{33}, dielectric susceptibility a, elastic parameter c_{33}, sound-pressure amplitude p_0^S, and model dimensions (length and width l, thickness h).

2. Flexoelectric model

For flexoelectric vector sensor, we assume that the external sound pressure p is also a plane wave propagating the normal vector direction $(0, 0, 1)$ of the upper surface. Then sound pressure on the upper surface $+\Omega$ is considered, which is shown as

$$p(t) = P_0^S e^{j\omega t}. \tag{A22}$$

The Euler-Bernoulli model is considered as our previous work [27], only the first-order vibration is considered, which is similar to the Rayleigh-Ritz method, where $w(x_2, t)$ is the transverse displacement of the neutral surface at point x_2 and time t. From this displacement field, u_3, u_2, and S_{22} are nonzero shown as

$$\begin{aligned}
u_3 &= w(x_2, t) = \xi(x_2) b(t),\\
u_2 &= -x_3 \frac{\partial w(x_2, t)}{\partial x_2} = -x_3 \xi'(x_2) b(t),\\
S_{22} &= \frac{\partial u_2}{\partial x_2} = -x_3 \xi'' b(t),
\end{aligned} \tag{A23}$$

where $\xi(x_2)$ for the symmetric Euler-Bernoulli cantilever beam is taken to be the eigenfunction [40], which is

$$\begin{aligned}
\xi(x_2) &= \cos\frac{\lambda}{l}x_2 - \cosh\frac{\lambda}{l}x_2 + \frac{\sin\lambda - \sinh\lambda}{\cos\lambda + \cosh\lambda}\\
&\quad \times \left(\sin\frac{\lambda}{l}x_2 - \sinh\frac{\lambda}{l}x_2\right).
\end{aligned} \tag{A24}$$

$\lambda = 1.87$ is the first root of the transcendental characteristic equation: $1 + \cos\lambda\cosh\lambda = 0$. $b(t)$ is unknown generalized coordinates. The nonzero strain gradient components are

$$\begin{aligned}
S_{22,3} &= -\frac{\partial^2 w}{\partial x_2^2} = -\xi'' b(t),\\
S_{22,2} &= -x_3 \frac{\partial^3 w}{\partial x_2^3} \ll S_{22,3},
\end{aligned} \tag{A25}$$

where the value of $S_{22,2}$ is much less than the value of $S_{22,3}$ due to the assumption. Therefore the component $S_{22,2}$ is ignored.

Given the assumptions, and setting $a = a_{33}$, $c_{22} = c_{2222}$ is the $2-2$ direction elastic parameter, $d_{32} = d_{322}$ is the piezoelectric constant, $f = f_{3223}$ and $g = g_{223223}$. The internal energy density Eq. (A4) is rewritten as

$$U_b = \frac{1}{2}aP_3^2 + \frac{1}{2}c_{22}S_{22}^2 - d_{32}PS_{22} - fPS_{22,3} + \frac{1}{2}gS_{22,3}^2. \tag{A26}$$

With Eq. (A26), then we can rewrite Eq. (A1) as

$$\begin{aligned}
&\int_{t_1}^{t_2} dt \int_V \Big\{-\rho\ddot{u}\delta u - aP\delta P + d_{32}S_{22}\delta P + fS_{22,3}\delta P\\
&\quad - c_{22}S_{22}\delta S_{22} + d_{32}P\delta S_{22} + fP\delta S_{22,3} - gS_{22,3}\delta S_{22,3}\\
&\quad + \frac{\partial D_3}{\partial x_3}\delta\phi - \frac{\partial\phi}{\partial x_3}\delta P\Big\} dV + \int_{t_1}^{t_2} dt \int_{\Omega^\pm} p\delta u dA = 0,
\end{aligned} \tag{A27}$$

where $D_3 = -\epsilon_0(\partial\phi/\partial x_3) + P$ denotes the electric displacement in the beam.

In Eq. (A27), δP is arbitrary, so we have

$$-aP + d_{32}S_{22} + fS_{22,3} - \frac{\partial \phi}{\partial x_3} = 0 \tag{A28}$$

and Maxwell equation

$$\frac{\partial D_3}{\partial x_3} = 0. \tag{A29}$$

Substituting Eq. (A28) into Eq. (A29), we further have

$$\frac{\partial^2 \phi}{\partial x_3^2} = -\frac{\partial E_3}{\partial x_3} = 0, \tag{A30}$$

where E_3 is the component of $\mathbf{E}$ in the x_3 direction. For the bulk coated with electrodes on the upper and lower surface of the sample. E_3 is the only nonzero component of $\mathbf{E}$. Equation (A30) indicates that the electric field is uniform across the thickness of the bulk. So the output voltage can be simply expressed as $E_3 = -v(t)/h$ where $v(t)$ is the voltage difference between upper and lower electrodes. Now dealing with the term associated with δu, δS_{22} and $\delta S_{22,3}$, Eq. (A27) can be further written as

$$\begin{aligned}\int_{t_1}^{t_2} dt \int_V \Big\{ & -\rho\ddot{u}\delta u - c_{22}S_{22}\delta S_{22} \\ & + d_{32}\left(-\frac{1}{a}\frac{v(t)}{h} + \frac{d_{32}S_{22}}{a} + \frac{fS_{22,3}}{a}\right)\delta S_{22} \\ & + f\left(-\frac{1}{a}\frac{v(t)}{h} + \frac{d_{32}}{S_{\ 22}}a + \frac{fS_{22,3}}{a}\right)\delta S_{22,3} \\ & - gS_{22,3}\delta S_{22,3}\Big\} dV + \int_{t_1}^{t_2} dt \int_{\partial\Omega^\pm} p\delta u dA = 0. \end{aligned}\tag{A31}$$

Due to the bending assumption of the small deformation cantilever beam, the integral of the portion containing the S_{22} term in the thickness direction of the cantilever beam is 0, that is, the piezoelectric effect does not contribute to the polarization of the cantilever beam $\int_V (*)S_{22}\, dV = 0$ [41].

The flexoelectric model also has a closed circuit where the charge density moving between the two electrodes is equal to the electric displacement at the surface where the electrode attached to. That means, the current $i(t)$ flowing through the resistor R equals the rate of the average electric displacement D_3, we also have an electrical governing equation:

$$\begin{aligned} i(t) = \frac{v(t)}{R} &= \frac{1}{h}\frac{d}{dt}\int_V \left(-\epsilon_0 \frac{v(t)}{h} + P\right) dV \\ &= -\frac{bl}{h}\left(\epsilon_0 + \frac{1}{a}\right)\dot{v}(t) + \frac{1}{h}\int_0^l \frac{fbh}{a}\frac{\partial^2 \dot{w}}{\partial x_3^2}\, dx_3. \end{aligned}\tag{A32}$$

Equations (A31) and (A32) are the governing equations of the bulk, then by substituting Eq. (A23) into those two equations, and adding a damped term $D\dot{b}(t)$, we can reduce the governing equations into the system of partial differential equations of time

$$\begin{aligned} & M^f \ddot{b}(t) + D\dot{b}(t) + K^f b(t) - \Theta^f v(t) = -p(t)l^2 \\ & C_f^f \dot{v}(t) + \frac{v(t)}{R} + \Theta^f \dot{b}(t) = 0, \end{aligned}\tag{A33}$$

where b is the upper-surface deflection amplitude that needs to be solved, M^f, K^f, Θ^f, C_f^f are equivalent mass parameter, stiffness parameter, flexoelectric coupling coefficients, and velocity coupling parameter, shown as follows:

$$\begin{aligned} M^f &= \rho bh \int_0^l \xi \times \xi \, dx_2, \\ K^f &= (EI)^* \int_0^l \xi'' \times \xi'' \, dx_2, \\ \Theta^f &= \frac{fbh}{ah}\int_0^l \xi'' \, dx_2, \\ C_f^f &= \frac{bl}{h}\left(\epsilon_0 + \frac{1}{a}\right), \end{aligned}\tag{A34}$$

and D is the damping constant, shown as

$$D = \mu M + \gamma K, \tag{A35}$$

where μ and γ are the constant of proportionality [42], which can be calculated as follows:

$$\begin{bmatrix}\gamma \\ \mu\end{bmatrix} = \frac{2\omega_1\omega_2}{\omega_1^2 - \omega_2^2}\begin{bmatrix}\dfrac{1}{\omega_2} & -\dfrac{1}{\omega_1} \\ -\omega_2 & \omega_1\end{bmatrix}\begin{bmatrix}\zeta_1 \\ \zeta_2\end{bmatrix}. \tag{A36}$$

ω_1 and ω_2 are the first two nature frequencies of the beam. The excitation in the system is provided by the sound pressure accepted by the upper surface of the model, which still can be written as

$$p = -P_0^S e^{j\omega t}. \tag{A37}$$

$b(t)$ and $v(t)$ can also be expressed as the harmonic response with frequency ω as follows:

$$b(t) = Be^{j\omega t}, \quad v(t) = Ve^{j\omega t}. \tag{A38}$$

Substituting Eqs. (A37) and (A38) into Eq. (A33), the unknown amplitudes B and V are

$$\begin{aligned} V ={}& j\omega\left(j\omega C_f^f+\frac{1}{R}\right)^{-1}\left(-\Theta^f\right)\\ &\times\Bigg[-\omega^2 M^f+j\omega(\mu M^f+\gamma K^f)+K^f\\ &+j\omega\left(j\omega C_f^f+\frac{1}{R}\right)^{-1}(\Theta^f)^2\Bigg]^{-1}P_0^S l^2,\\ B ={}& \left[-\omega^2 M^f+j\omega(\mu M^f+\gamma K^f)+K^f\right]^{-1}\\ &\times(P_0^S l^2+\Theta^f V). \end{aligned} \tag{A39}$$

3. Sound-pressure gradient sensitivity of two models

In calculations of the output voltage of the two models, the external force is reduced to an unary function of time. The function actually refers to the sound pressure value at $(0,0,0)$. A complete plane wave propagating along the x_3 direction should be expressed as

$$p(x_3,t)=P_0^S e^{j(\omega t-(\omega/c_0)x_1)}, \tag{A40}$$

where c_0 is the velocity of sound wave. The sound wave at $(0,0,0)$ is the same as in Eqs. (A7) and (A22): $p(x_3,t)|_{x_3=0}=P_0^S e^{j\omega t}$. The sound-pressure gradient level G_{fl} is defined as

$$G_{fl}=20\log_{10}\frac{|V/(-j\omega P_0^S/c_0)|}{G_r}, \tag{A41}$$

where $G_r=1$ Vm/μPa is the reference level, $G_f=V/(-j\omega P_0^S/c_0)$ represents the sound-pressure gradient sensitivity along x_3 direction. and $-(j\omega P_0^S/c_0)$ is the component of the sound-pressure gradient in x_3 direction. By substituting Eqs. (A21) and (A40) into Eq. (A41), G_{fl} of the piezoelectric model is obtained, which is shown as

$$\begin{aligned} G_{fl} ={}& 20\log_{10}\Bigg\{\Bigg|c_0\left(j\omega C_f^p+\frac{1}{R}\right)^{-1}\Theta^p\\ &\times\left[\left(-\omega^2 M^p+K^p\right)\left(j\omega C_f^p+\frac{1}{R}\right)+j\omega(\Theta^p)^2\right]^{-1}\\ &\times\left(j\omega C_f^p+\frac{1}{R}\right)l^2\Bigg|G_r^{-1}\Bigg\}. \end{aligned} \tag{A42}$$

By substituting Eqs. (A39) and (A40) into Eq. (A41), G_{fl} of the flexoelectric model is obtained, which is shown as

$$\begin{aligned} G_{fl} ={}& 20\log_{10}\Bigg\{\Bigg|c_0\left(j\omega C_f^f+\frac{1}{R}\right)^{-1}\left(-\Theta^f\right)\\ &\times\Bigg[-\omega^2 M^f+j\omega(\mu M^f+\gamma K^f)+K^f\\ &+j\omega\left(j\omega C_f^f+\frac{1}{R}\right)^{-1}(\Theta^f)^2\Bigg]^{-1}l^2\Bigg|G_r^{-1}\Bigg\}. \end{aligned} \tag{A43}$$

[1] A. Shaw, A. Al-Shamma'a, S. Wylie, and D. Toal, in *2006 European Microwave Conference* (IEEE, New York, USA, 2006), p. 572.

[2] J. Heidemann, M. Stojanovic, and M. Zorzi, Underwater sensor networks: Applications, advances and challenges, Philos. Trans. R. Soc. A: Math. Phys. Eng. Sci. **370**, 158 (2012).

[3] W. A. Kuperman and P. Roux, in *Springer Handbook of Acoustics* (Springer, New York, USA, 2007), p. 149.

[4] R. Diamant and L. Lampe, Low probability of detection for underwater acoustic communication: A review, IEEE Access **6**, 19099 (2018).

[5] M. F. McKenna, D. Ross, S. M. Wiggins, and J. A. Hildebrand, Underwater radiated noise from modern commercial ships, J. Acoust. Soc. Am. **131**, 92 (2012).

[6] G. Marani and S. K. Choi, Underwater target localization, IEEE Robot. Autom. Mag. **17**, 64 (2010).

[7] X. Lurton, *An Introduction to Underwater Acoustics: Principles and Applications* (Springer Science & Business Media, London, UK, 2002).

[8] R. P. Hodges, *Underwater Acoustics: Analysis, Design and Performance of Sonar* (John Wiley & Sons, Chichester, UK, 2011).

[9] H. Helmholtz, The theory of Sound, Nature **17**, 430 (1878).

[10] Desen Yang, V. Gordienko, and Lianjin Hong, *Underwater Vector Sound Field Theory and Its Applications* (Science Press, Beijing, China, 2013).

[11] T. Požar and J. Možina, Measurement of Elastic Waves Induced by the Reflection of Light, Phys. Rev. Lett. **111**, 185501 (2013).

[12] T. A. Brzinski III and K. E. Daniels, Sounds of Failure: Passive Acoustic Measurements of Excited Vibrational Modes, Phys. Rev. Lett. **120**, 218003 (2018).

[13] H. Hanzawa, S. Yoshida, K. Wasa, and S. Tanaka, in *2015 Transducers-2015 18th International Conference on Solid-State Sensors, Actuators and Microsystems (TRANSDUCERS)* (IEEE, Anchorage, USA, 2015), p. 1338.

[14] T. Wang and C. Lee, in *2015 Transducers-2015 18th International Conference on Solid-State Sensors, Actuators and Microsystems (TRANSDUCERS)* (IEEE, Anchorage, USA, 2015), p. 666–669.

[15] J. W. Strutt and B. Rayleigh, *The Theory of Sound* (Dover, New York, USA, 1945).
[16] D. Potter and S. Murphy, Solution of the wave equation in a medium with a particular velocity variation, J. Acoust. Soc. Am. **34**, 963 (1962).
[17] P. G. Bergmann, The wave equation in a medium with a variable index of refraction, J. Acoust. Soc. Am. **17**, 329 (1946).
[18] A. Safari and E. K. Akdogan, *Piezoelectric and Acoustic Materials for Transducer Applications* (Springer Science & Business Media, New York, USA, 2008).
[19] N. Murayama, K. Nakamura, H. Obara, and M. Segawa, The strong piezoelectricity in polyvinylidene fluroide (PVDF), Ultrasonics **14**, 15 (1976).
[20] H. Y. Guney, Elastic properties and mechanical relaxation behaviors of PVDF (polyvinylidene fluoride) at temperatures between −20 and 100 °C and at 2 MHz ultrasonic frequency, J. Polym. Sci., Part B: Polym. Phys. **43**, 2862 (2005).
[21] B. Chu and D. Salem, Flexoelectricity in several thermoplastic and thermosetting polymers, Appl. Phys. Lett. **101**, 103905 (2012).
[22] A. Tagantsev, Piezoelectricity and flexoelectricity in crystalline dielectrics, Phys. Rev. B **34**, 5883 (1986).
[23] P. Zubko, G. Catalan, and A. K. Tagantsev, Flexoelectric effect in solids, Annu. Rev. Mater. Res. **43**, 387 (2013).
[24] S. Krichen and P. Sharma, Flexoelectricity: A perspective on an unusual electromechanical coupling, J. Appl. Mech. **83**, 030801 (2016).
[25] D. Lee, A. Yoon, S. Y. Jang, J.-G. Yoon, J.-S. Chung, M. Kim, J. F. Scott, and T. W. Noh, Giant Flexoelectric Effect in Ferroelectric Epitaxial Thin Films, Phys. Rev. Lett. **107**, 057602 (2011).
[26] C. Liu, S. Hu, and S. Shen, Effect of flexoelectricity on electrostatic potential in a bent piezoelectric nanowire, Smart Mater. Struct. **21**, 115024 (2012).
[27] Q. Deng, M. Kammoun, A. Erturk, and P. Sharma, Nanoscale flexoelectric energy harvesting, Int. J. Solids. Struct. **51**, 3218 (2014).
[28] U. K. Bhaskar, N. Banerjee, A. Abdollahi, Z. Wang, D. G. Schlom, G. Rijnders, and G. Catalan, A flexoelectric microelectromechanical system on silicon, Nat. Nanotechnol. **11**, 263 (2016).
[29] X. Liang, S. Hu, and S. Shen, Nanoscale mechanical energy harvesting using piezoelectricity and flexoelectricity, Smart Mater. Struct. **26**, 035050 (2017).
[30] S. M. Park, B. Wang, S. Das, S. C. Chae, J.-S. Chung, J.-G. Yoon, L.-Q. Chen, S. M. Yang, and T. W. Noh, Selective control of multiple ferroelectric switching pathways using a trailing flexoelectric field, Nat. Nanotechnol. **13**, 366 (2018).
[31] W. Ma and L. E. Cross, Flexoelectric polarization of barium strontium titanate in the paraelectric state, Appl. Phys. Lett. **81**, 3440 (2002).
[32] C. A. Mizzi, A. Y. Lin, and L. D. Marks, Does Flexoelectricity Drive Triboelectricity?, Phys. Rev. Lett. **123**, 116103 (2019).
[33] F. Zhang, P. Lv, Y. Zhang, S. Huang, C.-M. Wong, H.-M. Yau, X. Chen, Z. Wen, X. Jiang, C. Zeng, *et al.*, Modulating the Electrical Transport in the Two-Dimensional Electron Gas at $LaAlO_3/SrTiO_3$ Heterostructures by Interfacial Flexoelectricity, Phys. Rev. Lett. **122**, 257601 (2019).
[34] K. Cordero-Edwards, H. Kianirad, C. Canalias, J. Sort, and G. Catalan, Flexoelectric Fracture-Ratchet Effect in Ferroelectrics, Phys. Rev. Lett. **122**, 135502 (2019).
[35] Q. Deng and S. Shen, The flexodynamic effect on nanoscale flexoelectric energy harvesting: A computational approach, Smart Mater. Struct. **27**, 105001 (2018).
[36] L. Zhaoqi, D. Qian, and s. Shengping, Flexoelectric energy harvesting using circular thin membranes, J. Appl. Mech. **87**, 091004 (2020).
[37] X. Wen, G. Yang, Q. Ma, Y. Tian, X. Liu, D. Xue, Q. Deng, and S. Shen, Flexoelectricity in compositionally graded $Ba_{1-x}Sr_xTiO_3$ ceramics, J. Appl. Phys. **130**, 074102 (2021).
[38] M. Menne, Global long-term mean land and sea surface temperatures, Tech. Rep., National Climatic Data Center, 2000.
[39] C. Van Loan, *Computational Frameworks for the Fast Fourier Transform* (SIAM, Philadelphia, USA, 1992), Vol. 10.
[40] A. Erturk and D. J. Inman, *Piezoelectric Energy Harvesting* (John Wiley & Sons, Chichester, UK, 2011).
[41] Q. Deng, S. Lv, Z. Li, K. Tan, X. Liang, and S. Shen, The impact of flexoelectricity on materials, devices, and physics, J. Appl. Phys. **128**, 080902 (2020).
[42] R. Clough and J. Penzien, *Dynamics of Structures* (McGraw Hill, New York, USA, 1993).